









Efficient Computation of Partial Elements in the Full-Wave Surface-PEEC Method

Francesca Di Murro, Daniele Romano , Maria De Lauretis ,
Ivana Kovacevic-Badstubner , *Senior Member, IEEE*, Luigi Lombardi , Ulrike Grossner , *Member, IEEE*,
Jonas Ekman , *Member, IEEE*, Fabrizio Frezza , *Senior Member, IEEE*,
and Giulio Antonini , *Senior Member, IEEE*

Abstract—The partial element equivalent circuit (PEEC) method provides an electromagnetic model of interconnections and packaging structures in terms of standard circuit elements. The surface-based PEEC (S-PEEC) formulation can reduce the number of unknowns compared to the standard volume-based PEEC (V-PEEC) method. This reduction is of particular use in the case of high-speed circuits and high-switching power electronics, where the bandwidth extends from low frequencies to the GHz range. In this article, the S-PEEC formulation is revised and cast in a matrix form. The main novelty is that the interaction integrals involving the curl of the magnetic and electric vector potentials are computed through the Taylor series expansion of the full-wave Green's function, leading to analytical forms that are rigorously derived. Therefore, the numerical integration is avoided, with a consequent reduction of the computation time. The proposed formulas are studied in terms of the frequency, size of the mesh, and distance between the basis function domains. Three examples are presented, confirming the accuracy of the proposed method compared to the V-PEEC method and surface-based numerical methods from literature.

Index Terms—Green's function, partial element equivalent circuit (PEEC) method, Taylor-series expansion.

I. INTRODUCTION

GENERAL circuit models of integrated circuit layouts and interconnections in a wide frequency range are critical to accurately predict circuit performance that could be degraded due to skin and proximity effects. The extraction of parasitics is

particularly relevant in high-frequency applications that involve the design of integrated circuits and on-chip and package interconnections, as well as in-power electronics applications. An accurate impedance extraction can be performed by using powerful numerical engines based on the finite element method [1], which resort to the meshing of the entire volume of the modeling domain and approximating the electromagnetic fields on this volume mesh. On the other hand, methods based on integral equations such as method of moments (MoM) and partial element equivalent circuit (PEEC) method [2]–[4] adopt a volumetric mesh based on the concept of the Green's function, and hence, differently from the FEM-based modeling, avoid the use of absorbing boundary conditions to approximate unbounded media. The PEEC method based on the volume equivalence principle is called volume-based PEEC (V-PEEC) [5]–[8], whereas the PEEC method based on the surface-equivalence principle is called surface-based PEEC (S-PEEC) [9]–[13]. Both of them can convert a multiconductor electromagnetic (EM) problem into a circuit-domain problem. However, the S-PEEC performs an electromagnetic computation only at the surface and not within the whole volume of the modeling domain. The surface formulation is particularly relevant for electrically thick objects, for which the V-PEEC formulation requires a large number of unknowns to correctly capture skin and proximity effects across a wide frequency range. S-PEEC models were first developed for conductors with surface impedance approximations [14], [15]. However, this approximation cannot be applied to dielectrics and it is valid only at higher frequencies, for which the conductor cross-sectional dimensions are larger than the skin-depth. In [16], an S-PEEC formulation for modeling arbitrarily shaped 3-D composite conductor and dielectric structures was presented as a systematic extension to the existing V-PEEC solvers. The proposed approach is based on the surface equivalence principle [17] and the so-called PMCHWT formulation [18], where both electric and magnetic field surface integral equations are used. This leads to electric and magnetic circuits which are coupled by mutual cross-couplings. The interaction integrals involve the full-wave Green's function in both the surrounding medium (e.g., air) and the modeling media including conductors, dielectrics, and/or magnetics, which support the surface electric and magnetic currents and charges. Special care has to be taken for the computational complexity and computational accuracy of the integrals [9]. In fact, the numerical computation

Manuscript received May 26, 2020; revised November 13, 2020; accepted January 9, 2021. Date of publication February 10, 2021; date of current version August 13, 2021. The work of Francesca Di Murro, Maria De Lauretis, Jonas Ekman, and Giulio Antonini was supported by Swedish Research Council under Grant 2018-05252. (*Corresponding author: Giulio Antonini.*)

Francesca Di Murro, Maria De Lauretis, and Jonas Ekman are with the Luleå University of Technology, 971 87 Lulea, Sweden (e-mail: francescadimurro@gmail.com; maria.de.lauretis@ltu.se; jonas.ekman@ltu.se).

Daniele Romano, Luigi Lombardi, and Giulio Antonini are with the UAQ EMC Laboratory, Department of Industrial and Information Engineering and Economics, University of L'Aquila, I-67100 L'Aquila, Italy (e-mail: daniele.romano.vis@gmail.com; luigilombardi89@gmail.com; giulio.antonini@uniuq.it).

Ivana Kovacevic-Badstubner and Ulrike Grossner are with the Advanced Power Semiconductor Laboratory, ETHZ, 8092 Zurich, Switzerland (e-mail: kovacevic@aps.ee.ethz.ch; ulrike.grossner@ethz.ch).

Fabrizio Frezza is with the Sapienza University, 00185 Rome, Italy (e-mail: fabrizio.frezza@uniroma1.it).

Color versions of one or more figures in this article are available at <https://doi.org/10.1109/TEMC.2021.3052358>.

Digital Object Identifier 10.1109/TEMC.2021.3052358

of these integrals is particularly challenging due to singularities and is time-consuming, especially for highly oscillating functions, which appear in the case of good conductors and a wide modeling bandwidth ranging from very low frequencies up to tens of GHz. Significant contributions have been proposed for the efficient computation of these integrals over triangular mesh [13], [19]–[22] in the framework of the MoM. A surface integral formulation using triangular mesh was proposed in [13] showing its advantage over the volume-based EM modeling. Conversely to the MoM, the PEEC formulation uses an orthogonal mesh. A boundary-integral-element (BIE) method using a differential surface admittance operator and an equivalent circuit derivation similar to the PEEC method was proposed in [12] for impedance extraction of 3-D interconnects using a rectangular cuboid mesh, which is an orthogonal mesh. The computation of dense matrices representing the interaction between basis-functions was based on the static Green's function, and the computational complexity of the interaction-integrals was not discussed in the article. In [23], simplified PEEC-based integral equations were obtained under the quasi-static assumption leading to a substantial reduction of the size of the subcircuits describing dielectrics. In [10], [11], the surface equivalent principle in the PEEC-based modeling framework with the full-wave Green's function was used to model rectangular multilayered structures. An accurate method to handle the singularity occurring in the interaction integrals is described in [24]. However, the integration is to be performed numerically.

In the PEEC formulation, orthogonal mesh (often referred as Manhattan-type mesh [8]) allows analytical calculation of the PEEC integrals [8], [25]. This can significantly reduce the computational complexity and makes the PEEC method attractive for fast and accurate EM modeling, which in turn can be used in optimization routines. Therefore, an orthogonal mesh is a preferable choice whenever geometrical simplifications are justified, which is the case for various engineering modeling tasks. In the context of the S-PEEC formulation employing rectangular surface mesh, the interaction integrals have been typically computed numerically and the analytical computation of these integrals has not been addressed in literature so far to the authors' best knowledge. The main focus of this article is the analytical computation of the interactions integrals occurring in the S-PEEC method. Accordingly, this article proposes a solution to avoid slow numerical calculation of the integrals involved in the S-PEEC formulation, which leads toward a computationally efficient S-PEEC modeling approach. In particular, analytical formulas for calculating the integrals occurring in the S-PEEC formulation based on the orthogonal surface mesh are presented. They are obtained by using the Taylor series expansion of the exponential term appearing in the Green's function. It is to be remarked that the fields of applicability of the proposed analytical formulas include the parasitic extraction of power electronic circuits, multilayered circuit boards [11], transmission lines [26], and 3-D on-chip interconnects [27], [28] where the orthogonal mesh is well suited.

The rest of this article is organized as follows. Section II briefly summarizes the S-PEEC formulation. Equations are re-organized in a matrix form and integrals to be computed are defined. In Section III, the analytical formulas for the surface

interaction integrals are presented. The range of applicability and the speed-up of the proposed formulas are discussed in Section IV and three numerical examples are presented pointing out the accuracy achieved. Finally, Section V concludes this article.

II. SURFACE PEEC FORMULATION

Given a 3D object, it is assumed that the surface separating the internal from the external problem is uniquely identified. The first region, named *region*₁, is the portion of the space limited by the surface of a closed 3-D object, and it is related to the internal problem. The second region, named *region*₂, is related to the external problem [17], [29]. The electric and magnetic fields in the two regions 1 and 2 can be written as

$$\mathbf{E}_{1,2}(\mathbf{r}) = -j\omega\mathbf{A}_{1,2}(\mathbf{r}) - \nabla\Phi_{1,2}^e(\mathbf{r}) + \frac{1}{\varepsilon_{1,2}}\nabla\times\mathbf{F}_{1,2}(\mathbf{r}) \quad (1a)$$

$$\mathbf{H}_{1,2}(\mathbf{r}) = -j\omega\mathbf{F}_{1,2}(\mathbf{r}) - \nabla\Phi_{1,2}^m(\mathbf{r}) + \frac{1}{\mu_{1,2}}\nabla\times\mathbf{A}_{1,2}(\mathbf{r}) \quad (1b)$$

where

$$\mathbf{A}_{1,2}(\mathbf{r}) = \mu_{1,2} \int_S G_{1,2}(\mathbf{r}, \mathbf{r}') \mathbf{J}_{s_{1,2}}(\mathbf{r}') ds' \quad (2a)$$

$$\mathbf{F}_{1,2}(\mathbf{r}) = \varepsilon_{1,2} \int_S G_{1,2}(\mathbf{r}, \mathbf{r}') \mathbf{M}_{s_{1,2}}(\mathbf{r}') ds' \quad (2b)$$

$$\Phi_{1,2}^e(\mathbf{r}) = \frac{1}{\varepsilon_{1,2}} \int_S G_{1,2}(\mathbf{r}, \mathbf{r}') q_{s_{1,2}}^e(\mathbf{r}') ds' \quad (2c)$$

$$\Phi_{1,2}^m(\mathbf{r}) = \frac{1}{\mu_{1,2}} \int_S G_{1,2}(\mathbf{r}, \mathbf{r}') q_{s_{1,2}}^m(\mathbf{r}') ds'. \quad (2d)$$

The Green's function $G_{1,2}(\mathbf{r}, \mathbf{r}')$ reads

$$G_{1,2}(\mathbf{r}, \mathbf{r}') = \frac{1}{4\pi} \frac{e^{-j\beta_{1,2}|\mathbf{r}-\mathbf{r}'|}}{|\mathbf{r}-\mathbf{r}'|}. \quad (3)$$

where

$$\beta_{1,2} = \omega\sqrt{\mu_{1,2}\varepsilon_{1,2}} \quad (4)$$

where $\mu_i, \varepsilon_i, i = 1, 2$, are the complex permeability and permittivity of the two regions. In the following, the dependence on $j\omega$ of the various matrices is omitted for the sake of simplicity.

Denoting with $\mathbf{E}_1^{inc}(\mathbf{r})$, $\mathbf{H}_1^{inc}(\mathbf{r})$, $\mathbf{E}_2^{inc}(\mathbf{r})$, and $\mathbf{H}_2^{inc}(\mathbf{r})$ the incident electric and magnetic fields in *region*₁ and *region*₂, respectively, the surface equivalence principle enforces the following boundary conditions:

$$\hat{\mathbf{n}} \times \left[\mathbf{E}_1(\mathbf{r}) + \mathbf{E}_1^{inc}(\mathbf{r}) \right] = \hat{\mathbf{n}} \times \left[\mathbf{E}_2(\mathbf{r}) + \mathbf{E}_2^{inc}(\mathbf{r}) \right]_{\mathbf{r} \in S} \quad (5a)$$

$$\hat{\mathbf{n}} \times \left[\mathbf{H}_1(\mathbf{r}) + \mathbf{H}_1^{inc}(\mathbf{r}) \right] = \hat{\mathbf{n}} \times \left[\mathbf{H}_2(\mathbf{r}) + \mathbf{H}_2^{inc}(\mathbf{r}) \right]_{\mathbf{r} \in S}. \quad (5b)$$

The electric and magnetic fields in (5) are expressed in terms of magnetic and electric vector and scalar potentials (2). They are referred to as surface-electric field integral equation (s-EFIE) and surface-magnetic field integral equation (s-MFIE), respectively. The continuity equations for the electric current and magnetic densities read as

$$\nabla \cdot \mathbf{J}_{s_{1,2}}(\mathbf{r}) = -j\omega q_{s_{1,2}}^e(\mathbf{r}) \quad (6a)$$

$$\nabla \cdot \mathbf{M}_{s_{1,2}}(\mathbf{r}) = -j\omega q_{s_{1,2}}^m(\mathbf{r}). \quad (6b)$$

The equivalent electrical and magnetic current densities on two sides of the same surface are related by

$$\mathbf{J}_{s_2}(\mathbf{r}) = -\mathbf{J}_{s_1}(\mathbf{r}) \quad \mathbf{M}_{s_2}(\mathbf{r}) = -\mathbf{M}_{s_1}(\mathbf{r}). \quad (7)$$

From (6) and (7), it is evident that similar boundary conditions hold for the electrical and magnetic surface charge densities

$$q_{s_2}^e(\mathbf{r}) = -q_{s_1}^e(\mathbf{r}) \quad q_{s_2}^m(\mathbf{r}) = -q_{s_1}^m(\mathbf{r}). \quad (8)$$

The surface S is meshed using two dual grids, referred in the following as ‘‘primal’’ and ‘‘dual’’ grids, for electric/magnetic currents and electric/magnetic charges, respectively. The electric and magnetic quantities are expanded using pulse basis function

$$\mathbf{b}_\ell(\mathbf{r}) = \begin{cases} \frac{\hat{\mathbf{u}}_\ell}{w_\ell} & \text{if } \mathbf{r} \in S_\ell \\ \mathbf{0} & \text{otherwise} \end{cases} \quad (9)$$

where $\hat{\mathbf{u}}_\ell$ is the unit vector indicating the current orientation on surface S_ℓ , where ℓ indicates the ℓ th surface element. w_ℓ is the width of the ℓ th elementary surface orthogonal to the direction in which the currents J_{s_ℓ} and M_{s_ℓ} flow.

Similarly, the basis functions used to expand the charge densities are

$$p_\ell(\mathbf{r}) = \begin{cases} \frac{1}{S_\ell} & \text{if } \mathbf{r} \in S_\ell \\ 0 & \text{otherwise} \end{cases} \quad (10)$$

where S_ℓ is the area of the ℓ th elementary surface where charges Q_ℓ^e and Q_ℓ^m are located.

Such choice of the basis functions assumes uniform electrical/magnetic current and charge densities over the elementary patches of the two grids:

$$J_{s_\ell} = \frac{I_\ell}{w_\ell}; \quad M_{s_\ell} = \frac{M_\ell}{w_\ell} \quad (11a)$$

$$q_{s_\ell}^e = \frac{Q_\ell^e}{S_\ell}; \quad q_{s_\ell}^m = \frac{Q_\ell^m}{S_\ell} \quad (11b)$$

where the weights I_ℓ and M_ℓ represent the electric/magnetic current flowing on the surface S_ℓ with orientation as defined by $\hat{\mathbf{u}}_\ell$ and $Q_\ell^{e,m}$ represents the surface electric and magnetic surface charge on the generic patch of the mesh.

Then, the Galerkin testing process is applied. To this aim, the following inner products are computed for each term of the s-EFIE/s-MFIE (5) and the continuity equations (6), respectively:

$$\langle \mathbf{f}(\mathbf{r}), \mathbf{b}_k(\mathbf{r}) \rangle = \frac{1}{w_k} \int_{S_k} \mathbf{f}(\mathbf{r}) \cdot \hat{\mathbf{u}}_k(\mathbf{r}) ds, \quad k = 1 \cdots N_s^p \quad (12a)$$

$$\langle g(\mathbf{r}), p_j(\mathbf{r}) \rangle = \int_{S_j} g(\mathbf{r}) \cdot p_j(\mathbf{r}) ds, \quad j = 1 \cdots N_s^d \quad (12b)$$

where N_s^p and N_s^d are the number of patches in the two grids.

Using expressions (1a) and (1b), the tested s-EFIE and s-MFIE are

$$0 = \frac{1}{w_k} \int_{S_k} \left\{ \left[\mathbf{E}_2^{inc}(\mathbf{r}) - \mathbf{E}_1^{inc}(\mathbf{r}) \right] + j\omega \left[\mathbf{A}_1(\mathbf{r}) - \mathbf{A}_2(\mathbf{r}) \right] \right. \\ \left. + \nabla \left[\Phi_1^e(\mathbf{r}) - \Phi_2^e(\mathbf{r}) \right] + \left[\frac{1}{\varepsilon_1} \nabla \times \mathbf{F}_1(\mathbf{r}) - \frac{1}{\varepsilon_2} \nabla \times \mathbf{F}_2(\mathbf{r}) \right] \right\} \cdot \hat{\mathbf{u}}_k(\mathbf{r}) ds \quad (13a)$$

$$0 = \frac{1}{w_k} \int_{S_k} \left\{ \left[\mathbf{H}_2^{inc}(\mathbf{r}) - \mathbf{H}_1^{inc}(\mathbf{r}) \right] + j\omega \left[\mathbf{F}_1(\mathbf{r}) - \mathbf{F}_2(\mathbf{r}) \right] \right. \\ \left. + \nabla \left[\Phi_1^m(\mathbf{r}) - \Phi_2^m(\mathbf{r}) \right] + \left[\frac{1}{\mu_1} \nabla \times \mathbf{A}_1(\mathbf{r}) - \frac{1}{\mu_2} \nabla \times \mathbf{A}_2(\mathbf{r}) \right] \right\} \cdot \hat{\mathbf{u}}_k(\mathbf{r}) ds \quad (13b)$$

for $i = 1, \dots, N_s^p$, where the testing functions are assumed identical to the basis functions. Since the surface mesh for electrical and magnetization currents is the dual of that for electric and magnetic charges, we denote as \mathbf{H}^C and \mathbf{K}^C the matrices computed by integrating the Green’s function (3) and its curl in (13) over the currents pertinent domains of the primal grid, respectively. We denote as \mathbf{H}^Q the integrals referred to the surface electrical and magnetic charges computed on the elementary patches of the dual grid.

The generic element k, ℓ of the matrices H and K is computed as

$$H_{1,2}^C(k, \ell) = \frac{1}{4\pi w_k w_\ell} \int_{S_k} \int_{S_\ell} \left[\frac{e^{-j\beta_{1,2}|\mathbf{r}-\mathbf{r}'|}}{|\mathbf{r}-\mathbf{r}'|} \hat{\mathbf{u}}_\ell(\mathbf{r}') \right] \\ \cdot \hat{\mathbf{u}}_k(\mathbf{r}) ds ds' \quad (14a)$$

$$K_{1,2}^C(k, \ell) = \frac{1}{4\pi w_k w_\ell} \int_{S_k} \int_{S_\ell} \left[\nabla \times \frac{e^{-j\beta_{1,2}|\mathbf{r}-\mathbf{r}'|}}{|\mathbf{r}-\mathbf{r}'|} \hat{\mathbf{u}}_\ell(\mathbf{r}') \right] \\ \cdot \hat{\mathbf{u}}_k(\mathbf{r}) ds ds' \quad (14b)$$

with $k, \ell = 1 \cdots N_s^p$. By applying the Galerkin’s testing procedure to (2c) and (2d), the corresponding matrix form reads

$$\Phi_{1,2}^e = \frac{1}{\varepsilon_{1,2}} \mathbf{H}_{1,2}^Q \mathbf{Q}_{1,2}^e = \mathbf{P}_{1,2}^e \mathbf{Q}_{1,2}^e \quad (15a)$$

$$\Phi_{1,2}^m = \frac{1}{\mu_{1,2}} \mathbf{H}_{1,2}^Q \mathbf{Q}_{1,2}^m = \mathbf{P}_{1,2}^m \mathbf{Q}_{1,2}^m \quad (15b)$$

where the k, ℓ th entry of $\mathbf{H}_{1,2}^Q$ is

$$H_{1,2}^Q(k, \ell) = \frac{1}{4\pi S_k S_\ell} \int_{S_k} \int_{S_\ell} \frac{e^{-j\beta_{1,2}|\mathbf{r}-\mathbf{r}'|}}{|\mathbf{r}-\mathbf{r}'|} ds ds' \quad (16)$$

with $k, \ell = 1 \cdots N_s^d$.

The primal and dual surfaces are meshed using a Manhattan-type (rectangular) mesh. Manhattan-type meshes have become popular in the V-PEEC formulation because they allow obtaining analytical formulas of partial elements, namely partial inductances and coefficients of potentials [5], [6] under the quasi-static assumption. In the V-PEEC formulation in [25], [30], Taylor's expansion of the full-wave Green's function with analytical formulas has been used. In this article, a similar approach is followed.

Analytical formulas for the calculation of partial elements in the V-PEEC formulation including the full-wave Green's function have been handled by means of the Taylor's expansion in [25], [30].

In the following, each patch is uniquely associated with a node in an equivalent circuit network, and touching patches that share the same node have the same (unique) potential. The continuity of the potential across touching patches and the conservation of the charge are enforced with a reduction matrix \mathbf{T} acting on $\Phi_{1,2}^{e,m}$ and $\mathbf{Q}_{1,2}^{e,m}$ as follows:

$$\Phi_{1,2}^{(e,m)} = \mathbf{T} \tilde{\Phi}_{1,2}^{(e,m)} \quad (17a)$$

$$\tilde{\mathbf{Q}}_{1,2}^{(e,m)} = \mathbf{T}^T \mathbf{Q}_{1,2}^{(e,m)} \quad (17b)$$

$$\begin{aligned} \tilde{\Phi}_{1,2}^{(e,m)} &= \left(\mathbf{T}^T \mathbf{P}_{1,2}^{(e,m)-1} \mathbf{T} \right)^{-1} \tilde{\mathbf{Q}}_{1,2}^{(e,m)} = \\ &= \tilde{\mathbf{P}}_{1,2}^{(e,m)} \tilde{\mathbf{Q}}_{1,2}^{(e,m)}. \end{aligned} \quad (17c)$$

where the "tilde" denotes the reduced potentials and charges. Hence, the electric and magnetic charges can be related to the electric and magnetic potentials as

$$\begin{aligned} \tilde{\mathbf{Q}}_{1,2}^{(e,m)} &= \left(\mathbf{T}^T \mathbf{P}_{1,2}^{(e,m)-1} \mathbf{T} \right) \tilde{\Phi}_{1,2}^{(e,m)} = \\ &= \left[\tilde{\mathbf{P}}_{1,2}^{(e,m)} \right]^{-1} \tilde{\Phi}_{1,2}^{(e,m)}. \end{aligned} \quad (18)$$

By using the Galerkin's testing process and assuming constant basis functions over the elementary domains, the continuity equations (6) for the external and internal problems of both the electric and magnetic charges are rewritten as

$$-\mathbf{A}^T \mathbf{I} + j\omega \left[\tilde{\mathbf{P}}_1^{(e)} \right]^{-1} \tilde{\Phi}_1^{(e)} = \mathbf{I}_s \quad (19a)$$

$$\mathbf{A}^T \mathbf{I} + j\omega \left[\tilde{\mathbf{P}}_2^{(e)} \right]^{-1} \tilde{\Phi}_2^{(e)} = \mathbf{I}_s \quad (19b)$$

$$-\mathbf{A}^T \mathbf{M} + j\omega \left[\tilde{\mathbf{P}}_1^{(m)} \right]^{-1} \tilde{\Phi}_1^{(m)} = \mathbf{0} \quad (19c)$$

$$\mathbf{A}^T \mathbf{M} + j\omega \left[\tilde{\mathbf{P}}_2^{(m)} \right]^{-1} \tilde{\Phi}_2^{(m)} = \mathbf{0} \quad (19d)$$

where \mathbf{A} is the connectivity matrix [8] and \mathbf{I}_s is the electric current sources vector. Depending on the frequency of interest, the surface impedance approximation guarantees reasonable accuracy [31]. Given a generic conductor body, if the cross-sectional dimensions of the conductor are much larger than the effective skin depth for the defined frequency, i.e., the skin-effect is well developed, the surface impedance approximation is a valid assumption [16]. However, such a model is typically

accurate enough only at relatively high frequencies (above tens of MHz). The resulting model can be expressed in the time domain by approximating the surface impedance in a rational form in the complex plane [32]. If the dimension of the conductor and the operating frequency do not allow assuming the surface impedance approximation, the conductor can be modeled as a dielectric object with a complex permittivity given by

$$\varepsilon(\omega) = \varepsilon' \left(1 + \frac{\sigma}{j\omega\varepsilon'} \right) \quad (20)$$

where ε' is the real part of the permittivity of the surrounding dielectric.

Finally, using integrals (14) and (16), (13) can be rewritten as

$$j\omega \mathbf{L}_p^e \mathbf{I} + \mathbf{K} \mathbf{M} + \mathbf{A} \tilde{\Phi}_1^e - \mathbf{A} \tilde{\Phi}_2^e = \mathbf{V}_s^e \quad (21a)$$

$$-\mathbf{K} \mathbf{I} + j\omega \mathbf{L}_p^m \mathbf{M} + \mathbf{A} \tilde{\Phi}_1^m - \mathbf{A} \tilde{\Phi}_2^m = \mathbf{V}_s^m \quad (21b)$$

where matrices \mathbf{L}_p^e , \mathbf{L}_p^m , \mathbf{K} are

$$\mathbf{L}_p^e = \mu_1 \mathbf{H}_1^C + \mu_2 \mathbf{H}_2^C \quad (22a)$$

$$\mathbf{L}_p^m = \varepsilon_1 \mathbf{H}_1^C + \varepsilon_2 \mathbf{H}_2^C \quad (22b)$$

$$\mathbf{K} = \mathbf{K}_1^C + \mathbf{K}_2^C \quad (22c)$$

and the right-hand-side terms represent the excitations voltages

$$\mathbf{V}_{sk}^e = \frac{1}{w_k} \int_{S_k} [\mathbf{E}_1^{inc}(\mathbf{r}) - \mathbf{E}_2^{inc}(\mathbf{r})] \cdot \hat{\mathbf{u}}_k(\mathbf{r}) ds \quad (23a)$$

$$\mathbf{V}_{sk}^m = \frac{1}{w_k} \int_{S_k} [\mathbf{H}_1^{inc}(\mathbf{r}) - \mathbf{H}_2^{inc}(\mathbf{r})] \cdot \hat{\mathbf{u}}_k(\mathbf{r}) ds \quad (23b)$$

with $k = 1, \dots, N_s^p$.

Finally, a matrix block-elimination of (21) and (19) allows rewriting the equations in terms of the electric currents \mathbf{I} and electric potentials Φ_1^e of the exterior problem

$$\begin{bmatrix} \mathbf{Z}_s^{em} & \mathbf{A} \\ -\mathbf{A}^T & j\omega \tilde{\mathbf{C}}_1^e \end{bmatrix} \begin{bmatrix} \mathbf{I} \\ \Phi_1^e \end{bmatrix} = \begin{bmatrix} \mathbf{V}_s^{em} \\ \mathbf{I}_s \end{bmatrix} \quad (24)$$

where $\tilde{\mathbf{C}}_1^e = [\tilde{\mathbf{P}}_1^e]^{-1}$ and where the impedance matrix \mathbf{Z}_s^{em} and \mathbf{V}_s^{em} represent the equivalent surface impedance and the equivalent voltage source taking into account both the electric and magnetic surface phenomena, and are defined as

$$\mathbf{Z}_s^{em} = j\omega \mathbf{L}_p^e + \mathbf{K} \mathbf{T} \mathbf{K} + \mathbf{A} \frac{\tilde{\mathbf{P}}_2^e}{j\omega} \mathbf{A}^T \quad (25a)$$

$$\mathbf{V}_s^{em} = \mathbf{V}_s^e + \mathbf{K} \mathbf{T} \mathbf{V}_s^m + \mathbf{A} \frac{\tilde{\mathbf{P}}_2^e}{j\omega} \mathbf{I}_s \quad (25b)$$

$$\mathbf{T} = \left[j\omega \mathbf{L}_p^m + \frac{1}{j\omega} \mathbf{A} \left(\tilde{\mathbf{P}}_1^m + \tilde{\mathbf{P}}_2^m \right) \mathbf{A}^T \right]^{-1}. \quad (25c)$$

The system matrix (24) has a circuit interpretation, as depicted in Fig. 1.

III. ANALYTICAL COMPUTATIONS

Equation (14) requires the solution of two types of integrals

$$\mathcal{I}_{hh} = \int_S \int_{S'} \frac{\hat{\mathbf{u}}(\mathbf{r}') e^{-j\beta|\mathbf{r}-\mathbf{r}'|}}{|\mathbf{r}-\mathbf{r}'|} dS dS' \quad (26a)$$

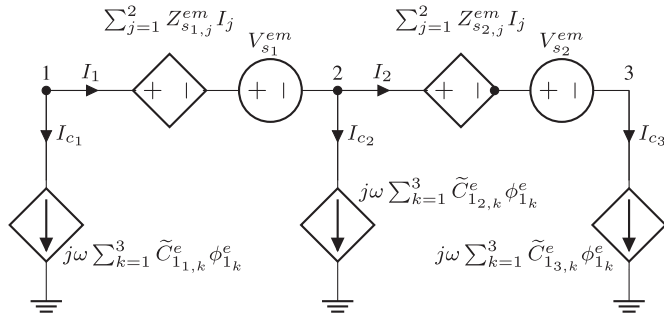


Fig. 1. Equivalent circuit model of the S-PEEC formulation (24) and (25) for a simple problem comprising two branches and three nodes.

$$\mathcal{I}_{h_k} = \int_S \int_{S'} \nabla \times \frac{\hat{\mathbf{u}}(\mathbf{r}') e^{-j\beta|\mathbf{r}-\mathbf{r}'|}}{|\mathbf{r}-\mathbf{r}'|} dS dS'. \quad (26b)$$

Integral (16) can be regarded as the scalar case of integral (26a).

In [25], the Green's function was computed by using its Taylor expansion that was then used to compute the integral (26a) in an efficient and accurate way, avoiding to resort to the computationally time-demanding numerical integration. In the following, we focus on the computation of integral (26b).

Under the assumption of a Manhattan-type mesh, from (26b), six transfer functions $h_{k_{y,x}}$, $h_{k_{z,x}}$, $h_{k_{x,y}}$, $h_{k_{z,y}}$, $h_{k_{x,z}}$, and $h_{k_{y,z}}$ can be defined as follows:

$$\mathcal{I}_{h_k} = \begin{cases} \hat{y} \int_S \int_{S'} \frac{\partial}{\partial z} \frac{e^{-j\beta R(x,y,z,x',y',z')}}{R(x,y,z,x',y',z')} ds' ds + \\ \quad \underbrace{h_{k_{y,x}}}_{\text{for } \hat{\mathbf{u}} = [\hat{x}, 0, 0]} \\ + \hat{z} \int_S \int_{S'} \frac{\partial}{\partial y} \frac{e^{-j\beta R(x,y,z,x',y',z')}}{R(x,y,z,x',y',z')} ds' ds \\ \quad \underbrace{h_{k_{z,x}}}_{\text{for } \hat{\mathbf{u}} = [\hat{x}, 0, 0]} \\ \hat{x} \int_S \int_{S'} \frac{\partial}{\partial z} \frac{e^{-j\beta R(x,y,z,x',y',z')}}{R(x,y,z,x',y',z')} ds' ds + \\ \quad \underbrace{h_{k_{x,y}}}_{\text{for } \hat{\mathbf{u}} = [0, \hat{y}, 0]} \\ + \hat{z} \int_S \int_{S'} \frac{\partial}{\partial x} \frac{e^{-j\beta R(x,y,z,x',y',z')}}{R(x,y,z,x',y',z')} ds' ds \\ \quad \underbrace{h_{k_{z,y}}}_{\text{for } \hat{\mathbf{u}} = [0, \hat{y}, 0]} \\ \hat{x} \int_S \int_{S'} \frac{\partial}{\partial y} \frac{e^{-j\beta R(x,y,z,x',y',z')}}{R(x,y,z,x',y',z')} ds' ds + \\ \quad \underbrace{h_{k_{x,z}}}_{\text{for } \hat{\mathbf{u}} = [0, 0, \hat{z}]} \\ + \hat{y} \int_S \int_{S'} \frac{\partial}{\partial x} \frac{e^{-j\beta R(x,y,z,x',y',z')}}{R(x,y,z,x',y',z')} ds' ds \\ \quad \underbrace{h_{k_{y,z}}}_{\text{for } \hat{\mathbf{u}} = [0, 0, \hat{z}]} \end{cases}$$

where

$$R(x,y,z,x',y',z') = \sqrt{(x-x')^2 + (y-y')^2 + (z-z')^2}. \quad (27)$$

Note that only one transfer function, e.g., $h_{k_{y,z}}$, is to be computed because the solutions for the remaining transfer functions are obtained by a suitable change of variable.

First, $h_{k_{y,z}}$ is rewritten in the equivalent form as

$$h_{k_{y,z}} = e^{-j\beta R_{cc}} \int_S \int_{S'} \frac{\partial}{\partial x} \frac{e^{-j\beta [R(x,y,z,x',y',z') - R_{cc}]} }{R(x,y,z,x',y',z')} ds' ds \quad (28)$$

being R_{cc} the center-to-center distance between the two surfaces.

Then, the term $e^{-j\beta [R(x,y,z,x',y',z') - R_{cc}]}$ in (28) is approximated with its third-order Taylor's expansion (29)

$$\begin{aligned} e^{-j\beta \hat{R}(x,y,z,x',y',z')} &\simeq 1 - j\beta \hat{R}(x,y,z,x',y',z') + \\ &- \frac{1}{2} \beta^2 \hat{R}(x,y,z,x',y',z')^2 + j \frac{1}{6} \beta^3 \hat{R}(x,y,z,x',y',z')^3 \end{aligned} \quad (29)$$

where $\hat{R}(x,y,z,x',y',z') = R(x,y,z,x',y',z') - R_{cc}$.

Finally, using the approximation (29) in (28), and after some algebraic manipulations, the $h_{k_{y,z}}$ can be written as

$$\begin{aligned} h_{k_{y,z}} &\simeq e^{-j\beta R_{cc}} \left[h_{k_{y,z}}^{QS} + j\beta h_{k_{y,z}}^{QS} R_{cc} + \right. \\ &+ \beta^2 \left(-\frac{1}{2} h_{k_{y,z}}^{QS} R_{cc}^2 + \frac{1}{2} h_{k_{y,z}}^{o2} \right) + \\ &\left. + j\beta^3 \left(-\frac{1}{6} h_{k_{y,z}}^{QS} R_{cc}^3 + \frac{1}{2} h_{k_{y,z}}^{o2} R_{cc} - \frac{1}{6} h_{k_{y,z}}^{o3} \right) \right] \end{aligned} \quad (30)$$

where

$$h_{k_{y,z}}^{QS} = \int_S \int_{S'} \frac{\partial}{\partial x} \frac{1}{R(x,y,z,x',y',z')} ds' ds \quad (31a)$$

$$h_{k_{y,z}}^{o2} = - \int_S \int_{S'} \frac{\partial}{\partial x} R(x,y,z,x',y',z') ds' ds \quad (31b)$$

$$h_{k_{y,z}}^{o3} = - \int_S \int_{S'} \frac{\partial}{\partial x} R(x,y,z,x',y',z')^2 ds' ds. \quad (31c)$$

The analytical solution for integrals in (31) is provided in the next section for a simple geometrical configuration of two surfaces in the space. In fact, the solution for other geometrical configuration can be simply derived by a suitable change of variable.

A. Analytical Solution for $h_{k_{y,z}}$: Case 1

The analytical solution for the first cases is derived using two surfaces S and S' lying on the $x-y$ plane, where the surface S is defined by four vertices (x_1, y_1, z_1) , (x_2, y_1, z_1) , (x_1, y_2, z_1) , and (x_2, y_2, z_1) with $x_1 < x_2$ and $y_1 < y_2$, and the surface S' by the vertices (x_3, y_3, z_3) , (x_4, y_3, z_3) , (x_3, y_4, z_3) , and (x_4, y_4, z_3) with $x_3 < x_4$ and $y_3 < y_4$. In this case, the analytical solution for $h_{k_{y,z}}^{QS}$, defined in (31a), is given by

$$h_{k_{y,z}}^{QS} = \sum_{i=1}^2 \sum_{j=1}^2 \sum_{m=3}^4 \sum_{n=3}^4 (-1)^{i+j+m+n} \sum_{k=1}^4 \gamma_k \quad (32)$$

where

$$\gamma_1 = s_y s_z \arctan \left(\frac{s_x s_y}{s_z R} \right) \quad (33a)$$

$$\gamma_2 = -s_x s_y \operatorname{arctanh} \left(\frac{s_y}{R} \right) \quad (33b)$$

$$\gamma_3 = -\frac{1}{2}(s_y^2 - s_z^2) \log(s_x + R) \quad (33c)$$

$$\gamma_4 = \frac{1}{2} s_x R \quad (33d)$$

and

$$R = \sqrt{s_x^2 + s_y^2 + s_z^2} \quad (34a)$$

$$s_x = x_i - x_m \quad (34b)$$

$$s_y = y_j - y_n \quad (34c)$$

$$s_z = z_1 - z_3. \quad (34d)$$

By using the same definition in (34), the analytical solutions for $h_{k_{y,z}}^{o2}$, in (31b), and $h_{k_{y,z}}^{o3}$, in (31c), are derived

$$h_{k_{y,z}}^{o2} = \sum_{i=1}^2 \sum_{j=1}^2 \sum_{m=3}^4 \sum_{n=3}^4 (-1)^{i+j+m+n} \sum_{k=1}^4 \gamma_k \quad (35)$$

where

$$\gamma_1 = -\frac{1}{3} s_y s_z^3 \arctan \left(\frac{s_x s_y}{s_z R} \right) \quad (36a)$$

$$\gamma_2 = \frac{1}{24} (s_y^4 + 6s_y^2 s_z^2 - 3s_z^4) \log(s_x + R) \quad (36b)$$

$$\gamma_3 = \frac{1}{6} s_x s_y (s_x^2 + 3s_z^2) \log(s_y + R) \quad (36c)$$

$$\gamma_4 = \frac{1}{24} (-2s_x^2 + 3s_y^2 - 5s_z^2) R. \quad (36d)$$

$$h_{k_{y,z}}^{o3} = \sum_{i=1}^2 \sum_{j=1}^2 \sum_{m=3}^4 \sum_{n=3}^4 (-1)^{i+j+m+n} s_x^3 s_y^2. \quad (37)$$

B. Analytical Solution for $h_{k_{y,z}}$: Case 2

In case 2, a surface S lying on the $x - y$ plane and a surface S' lying on the $z - x$ plane are considered. The surface S is defined by four vertices (x_1, y_1, z_1) , (x_2, y_1, z_1) , (x_1, y_2, z_1) , and (x_2, y_2, z_1) with $x_1 < x_2$ and $y_1 < y_2$. Similarly, four vertices (x_3, y_3, z_3) , (x_4, y_3, z_3) , (x_3, y_3, z_4) , and (x_4, y_3, z_4) with $x_3 < x_4$ and $z_3 < z_4$ represent the surface S' . The analytical solution for $h_{k_{y,z}}^{QS}$, in (31a), is derived as

$$h_{k_{y,z}}^{QS} = \sum_{i=1}^2 \sum_{j=1}^2 \sum_{m=3}^4 \sum_{n=3}^4 (-1)^{i+j+m+n} \sum_{k=1}^6 \gamma_k \quad (38)$$

where

$$\gamma_1 = -s_y s_z \log(s_x + R) \quad (39a)$$

$$\gamma_2 = -s_x s_z \log(s_y + R) \quad (39b)$$

$$\gamma_3 = -s_x s_y \log(s_z + R) \quad (39c)$$

$$\gamma_4 = \frac{1}{2} s_z^2 \arctan \left(\frac{s_x s_y}{s_z R} \right) \quad (39d)$$

$$\gamma_5 = \frac{1}{2} s_y^2 \arctan \left(\frac{s_x s_z}{s_y R} \right) \quad (39e)$$

$$\gamma_6 = \frac{1}{2} s_x^2 \arctan \left(\frac{s_y s_z}{s_x R} \right) \quad (39f)$$

and where

$$R = \sqrt{s_x^2 + s_y^2 + s_z^2} \quad (40a)$$

$$s_x = x_i - x_m \quad (40b)$$

$$s_y = y_j - y_3 \quad (40c)$$

$$s_z = z_1 - z_n. \quad (40d)$$

By using the same definition in (40), the analytical solutions for $h_{k_{y,z}}^{o2}$, in (31b), and for $h_{k_{y,z}}^{o3}$, defined in (31c), are given by (41) and (43)

$$h_{k_{y,z}}^{o2} = \sum_{i=1}^2 \sum_{j=1}^2 \sum_{m=3}^4 \sum_{n=3}^4 (-1)^{i+j+m+n} \sum_{k=1}^7 \gamma_k \quad (41)$$

where

$$\gamma_1 = \frac{1}{4} s_x s_y s_z R \quad (42a)$$

$$\gamma_2 = -\frac{1}{12} s_z^4 \arctan \left(\frac{s_x s_y}{s_z R} \right) \quad (42b)$$

$$\gamma_3 = -\frac{1}{12} s_y^4 \arctan \left(\frac{s_x s_z}{s_y R} \right) \quad (42c)$$

$$\gamma_4 = -\frac{1}{12} s_x^4 \arctan \left(\frac{s_y s_z}{s_x R} \right) \quad (42d)$$

$$\gamma_5 = \frac{1}{6} s_y s_z (s_y^2 + s_z^2) \log(s_x + R) \quad (42e)$$

$$\gamma_6 = \frac{1}{6} s_x s_z (s_x^2 + s_z^2) \log(s_y + R) \quad (42f)$$

$$\gamma_7 = \frac{1}{6} s_y s_x (s_y^2 + s_x^2) \log(s_z + R). \quad (42g)$$

$$h_{k_{y,z}}^{o3} = \sum_{i=1}^2 \sum_{j=1}^2 \sum_{m=3}^4 \sum_{n=3}^4 (-1)^{i+j+m+n} \frac{1}{3} s_x^3 s_y s_z. \quad (43)$$

C. Analytical Solution for $h_{k_{y,z}}$: Case 3

The analytical solution for $h_{k_{y,z}}$ is provided by using an example of a surface S defined by four vertices (x_1, y_1, z_1) , (x_2, y_1, z_1) , (x_1, y_2, z_1) , and (x_2, y_2, z_1) with $x_1 < x_2$ and $y_1 < y_2$, and a surface S' defined by vertices (x_3, y_3, z_3) , (x_3, y_4, z_3) , (x_3, y_3, z_4) , and (x_3, y_4, z_4) with $y_3 < y_4$ and $z_3 < z_4$. In a similar way as in the previous cases, the analytical solutions for $h_{k_{y,z}}^{QS}$, $h_{k_{y,z}}^{o2}$, and $h_{k_{y,z}}^{o3}$, from (31), are defined by (44), (47) and (49), respectively.

$$h_{k_{y,z}}^{QS} = \sum_{i=1}^2 \sum_{j=1}^2 \sum_{m=3}^4 \sum_{n=3}^4 (-1)^{i+j+m+n} \sum_{k=1}^4 \gamma_k \quad (44)$$

where

$$\gamma_1 = s_x s_y \arctan\left(\frac{s_y s_z}{s_x R}\right) \quad (45a)$$

$$\gamma_2 = -s_y s_z \operatorname{arctanh}\left(\frac{s_y}{R}\right) \quad (45b)$$

$$\gamma_3 = -\frac{1}{2}(s_y^2 - s_x^2) \log(s_z + R) \quad (45c)$$

$$\gamma_4 = \frac{1}{2} s_z R \quad (45d)$$

and where

$$R = \sqrt{s_x^2 + s_y^2 + s_z^2} \quad (46a)$$

$$s_x = x_i - x_3 \quad (46b)$$

$$s_y = y_j - y_m \quad (46c)$$

$$s_z = z_1 - z_n. \quad (46d)$$

$$h_{k_{y,z}}^{o2} = \sum_{i=1}^2 \sum_{j=1}^2 \sum_{m=3}^4 \sum_{n=3}^4 (-1)^{i+j+m+n} \sum_{k=1}^6 \gamma_k \quad (47)$$

where

$$\gamma_1 = \frac{1}{3} s_x^3 s_y \arctan\left(\frac{s_z}{s_x}\right) \quad (48a)$$

$$\gamma_2 = -\frac{1}{3} s_x^3 s_y \arctan\left(\frac{s_y s_z}{s_x R}\right) \quad (48b)$$

$$\gamma_3 = \frac{1}{6} s_y s_z (s_z^2 + 3s_x^2) \log(s_y + R) \quad (48c)$$

$$\gamma_4 = \frac{1}{24} (-3s_x^4 + 6s_x^2 s_y^2 + s_y^4) \log(s_z + R) \quad (48d)$$

$$\gamma_5 = -\frac{1}{24} s_z R (2s_z^2 - 3s_y^2 + 5s_x^2) \quad (48e)$$

$$\gamma_6 = s_x^2 s_y s_z + \frac{1}{6} s_y s_z^3. \quad (48f)$$

$$h_{k_{y,z}}^{o3} = \sum_{i=1}^2 \sum_{j=1}^2 \sum_{m=3}^4 \sum_{n=3}^4 (-1)^{i+j+m+n} \frac{1}{2} s_x^2 s_y^2 s_z. \quad (49)$$

D. Analytical Solution for $h_{k_{y,z}}$: Case 4

In this last case, two surfaces S and S' lie on the $y-z$ plane. The surface S is defined by the vertices (x_1, y_1, z_1) , (x_1, y_2, z_1) , (x_1, y_1, z_2) , and (x_1, y_2, z_2) with $y_1 < y_2$ and $z_1 < z_2$, and the surface S' by (x_3, y_3, z_3) , (x_3, y_4, z_3) , (x_3, y_3, z_4) , and (x_3, y_4, z_4) with $y_3 < y_4$ and $z_3 < z_4$. In this case, the analytical solution for $h_{k_{y,z}}^{QS}$ is defined by (50). By using the same definition in (52), the analytical solutions for $h_{k_{y,z}}^{o2}$, and $h_{k_{y,z}}^{o3}$ from (31), are derived as (53) and (55).

$$h_{k_{y,z}}^{QS} = \sum_{i=1}^2 \sum_{j=1}^2 \sum_{m=3}^4 \sum_{n=3}^4 (-1)^{i+j+m+n} \sum_{k=1}^4 \gamma_k \quad (50)$$

where

$$\gamma_1 = s_y s_z \arctan\left(\frac{s_y s_z}{s_x \sqrt{s_x^2 + s_y^2 + s_z^2}}\right) \quad (51a)$$

$$\gamma_2 = s_x s_y \operatorname{arctanh}\left(\frac{\sqrt{s_x^2 + s_y^2 + s_z^2}}{s_y}\right) \quad (51b)$$

$$\gamma_3 = s_x s_z \log\left(s_z + \sqrt{s_x^2 + s_y^2 + s_z^2}\right) \quad (51c)$$

$$\gamma_4 = -s_x \sqrt{s_x^2 + s_y^2 + s_z^2} \quad (51d)$$

and where

$$R = \sqrt{s_x^2 + s_y^2 + s_z^2} \quad (52a)$$

$$s_x = x_1 - x_3 \quad (52b)$$

$$s_y = y_i - y_m \quad (52c)$$

$$s_z = z_j - z_n. \quad (52d)$$

$$h_{k_{y,z}}^{o2} = \sum_{i=1}^2 \sum_{j=1}^2 \sum_{m=3}^4 \sum_{n=3}^4 (-1)^{i+j+m+n} \sum_{k=1}^4 \gamma_k \quad (53)$$

where

$$\gamma_1 = -s_y s_z s_x^2 \arctan\left(\frac{s_y s_z}{s_x R}\right) \quad (54a)$$

$$\gamma_2 = \frac{1}{2} s_x s_z (s_y^2 - s_x^2) \log(s_z + R) \quad (54b)$$

$$\gamma_3 = \frac{1}{2} s_x s_y (s_z^2 - s_x^2) \log(s_y + R) \quad (54c)$$

$$\gamma_4 = -\frac{1}{6} s_x (s_z^2 + s_y^2 - 2s_x^2) R. \quad (54d)$$

$$h_{k_{y,z}}^{o3} = \sum_{i=1}^2 \sum_{j=1}^2 \sum_{m=3}^4 \sum_{n=3}^4 (-1)^{i+j+m+n} \frac{1}{2} s_x s_y^2 s_z^2. \quad (55)$$

E. Tips for Integrals Evaluation

In this section, the solution for the singularities of all the analytical formulas in Section III is presented. In particular, the singularity of type $x \log\left(\sqrt{x^2 + y^2 + z^2}\right)$ is solved by using the following limit:

$$\lim_{x \rightarrow 0} \left[x \log\left(\sqrt{x^2 + y^2 + z^2}\right) \right] = 0. \quad (56)$$

The function $x^2 \tan^{-1}\left(\frac{yz}{x\sqrt{x^2 + y^2 + z^2}}\right)$ is evaluated as $x|x| \arctan2\left(\frac{yz}{|x|\sqrt{x^2 + y^2 + z^2}}\right)$, where the function $\arctan2$ is defined by (57), with $\tan^{-1}(q)$ representing the inverse tangent of

q computed in the range $[-\pi/2, \pi/2]$.

$$\arctan 2 \left(\frac{k}{m} \right) = \begin{cases} \tan^{-1} \left(\frac{k}{m} \right) & \text{if } m > 0 \\ \tan^{-1} \left(\frac{k}{m} \right) + \pi & \text{if } k \geq 0 \ \& \ m < 0 \\ \tan^{-1} \left(\frac{k}{m} \right) - \pi & \text{if } k < 0 \ \& \ m < 0 \\ \frac{\pi}{2} & \text{if } k > 0 \ \& \ m = 0 \end{cases} \quad (57)$$

A detailed description of for solving this type of singularity can be found in [30].

IV. NUMERICAL RESULTS

Formula (30) for $h_{k_{y,z}}$ is validated with numerical examples. The analytic evaluation of $h_{k_{y,z}}^{QS}$, $h_{k_{y,z}}^{o2}$, and $h_{k_{y,z}}^{o3}$, as derived in Sections III-A–III-D, is further improved by using a technique proposed in [33], increasing the calculation accuracy when dealing with surfaces characterized by large aspect ratios, e.g., length much higher than width. The reader is referred to [33] for all the details. This technique allows the suppression of one or more dimensions of integration, alleviating the computational complexity. The analytical solution for simpler double folded integrals (resulting from the applied technique) can be easily obtained from the solutions of the surface–surface integrals provided in Sections III-A–III-D by performing one or more derivatives with respect to the variables belonging to the suppressed dimensions of the integration.

A. Evaluation of the Range of Applicability

The evaluation of $h_{k_{y,z}}$, in (30), is performed in the frequency range [100 Hz – 1 THz] sampled by 12 logarithmically spaced frequency points for two square surfaces with the same area. The distance between the nearest edges of the surfaces is varied in the range [0 – 1] m for a total of 31 geometrical configurations. Additionally, the tests are performed for the edge size of the surfaces in the range from 1 μm to 1 mm. The integral (30) is compared in two different ways.

- 1) TAYLOR: The integrals are computed using the derived analytical formulas provided in Sections III-A–III-D by adopting the strategy proposed in [33];
- 2) NUMERICAL: The integral computation is based on the adaptive numerical Gaussian integration described in [34] with a relative threshold error of 10^{-6} .

All the computations have been performed using Matlab, and the integral computed with the two different approaches are precompiled as MEX files [35]. The CPU times for the calculation of $h_{k_{y,z}}$ are summarized in Table I, emphasizing the speed-up achieved by the TAYLOR approach. In particular, the speed-up is computed as the ratio between the CPU time required for computing the integrals using the NUMERICAL method and the CPU time spent for computing the same integrals when using the derived analytical formulas, i.e., the TAYLOR method. From Table I, it is evident the TAYLOR method outperforms the NUMERICAL method.

TABLE I
CPU TIMES REQUIRED FOR CALCULATING THE INTEGRALS BASED ON THE TAYLOR AND NUMERICAL APPROACHES FOR THE DESCRIBED TEST CASES OF 31 GEOMETRICAL CONFIGURATIONS EVALUATED IN THE FREQUENCY RANGE BETWEEN 10 Hz AND 1 THz AT 12 FREQUENCY SAMPLES

	edge length			
	1 μm	10 μm	100 μm	1 mm
NUMERICAL time	70 s	81 s	93 s	114 s
TAYLOR time	< 10 ms	< 10 ms	< 10 ms	< 10 ms
SPEED-UP	$8.7 \cdot 10^4 \times$	$9.3 \cdot 10^4 \times$	$9.6 \cdot 10^4 \times$	$1.2 \cdot 10^5 \times$

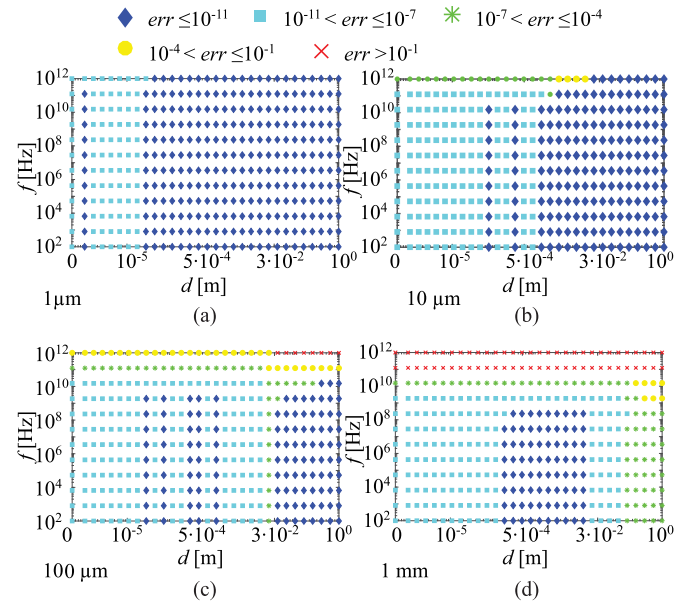


Fig. 2. Error evaluation for the transfer function $h_{k_{y,z}}$, defined in (30), for different surface sizes and for the external problem for the internal problem: (a) 1 μm , (b) 10 μm , (c) 100 μm , (d) 1 mm.

The accuracy of the proposed closed formulas are defined by the following relative error:

$$\epsilon = |h_{TAYLOR} - h_{NUMERICAL}| / |h_{NUMERICAL}|. \quad (58)$$

The relative errors of the $h_{k_{y,z}}$ computation for the external problem and internal problems are shown in Figs. 2 and 3, respectively. For the external problem, for a larger edge size of the surfaces, the accuracy of analytical formulas is decreasing at higher frequencies, due to the Taylor's expansion of the exponential term. However, the elementary mesh cells in practical applications are typically much smaller at higher frequencies, i.e., above 1 GHz, which is required to accurately capture the high-frequency effects. A similar behavior is shown also for the internal problem of conductors, but the TAYLOR approach fails at lower frequencies. Hence, the numerical integration for the internal problem is required in all the cases in which the error is higher than 0.1 % as reported in Fig. 3. The analytical solution of integrals occurring in the internal problems of conductors is under investigation and the results will be presented in forthcoming publications. It is important to point out that all the considerations made for $h_{k_{y,z}}^{QS}$ are valid also for the coefficients

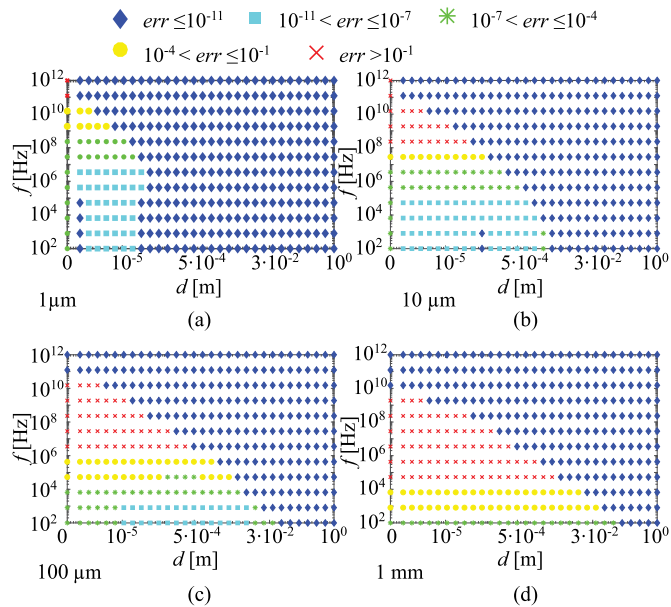


Fig. 3. Error evaluation for the transfer function $h_{k_y,z}$, defined in (30), for different surface sizes and for the internal problem for the internal problem: (a) 1 μm , (b) 10 μm , (c) 100 μm , (d) 1 mm.

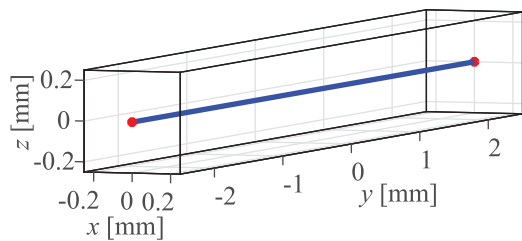


Fig. 4. Test example: a single copper bar.

of \mathbf{H} and \mathbf{P} matrices because they have an error similar to that reported in Figs. 2 and 3.

In the first example, a single copper bar is used to demonstrate the differences between S-PEEC and V-PEEC modeling. In particular, the FEM method requires to define a return path for the current, which would impact the modeling results. Therefore, the results were compared to low frequency ANSYS Q3D simulator, specialized for the extraction of partial inductances, resistances, and capacitances. Then, two more examples are taken from the literature in order to compare the proposed S-PEEC method with the other surface-based numerical techniques from literature mainly in terms of accuracy. In all the examples, a direct LU-based solver is used.

B. Single Copper Bar Example

In this example, a copper bar of size $0.5 \times 0.5 \times 5$ mm is considered. The geometry is depicted in Fig. 4 where the blue line represents the lumped current port. The ports are modeled as equipotential squares of 1.8 mm^2 centered around the red dots in Fig. 4. The port impedance, evaluated through different methods, is shown in Fig. 5, where

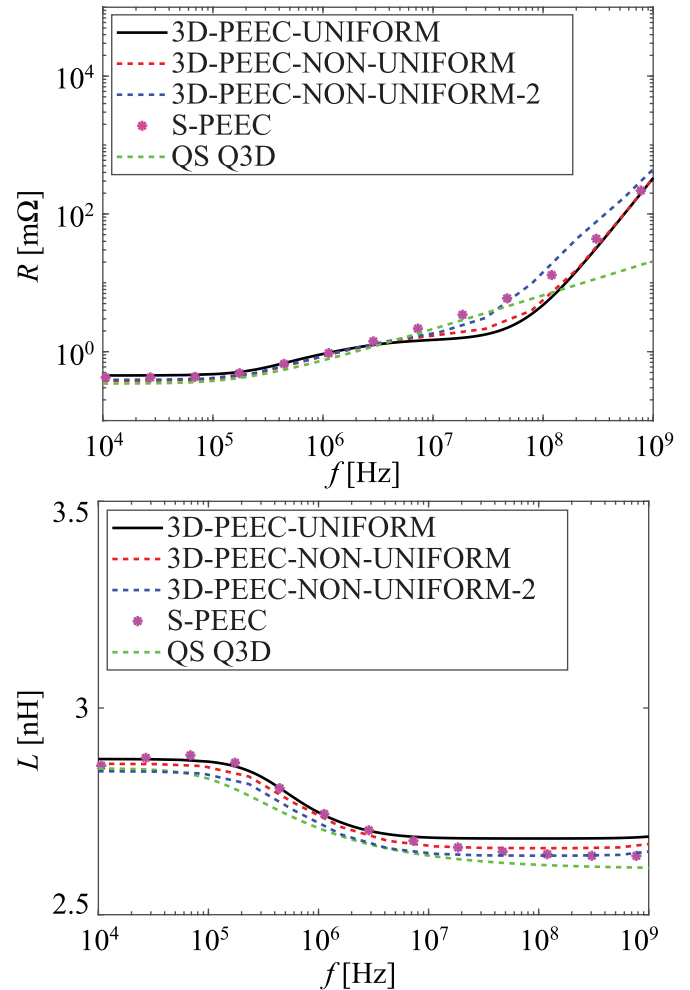


Fig. 5. Port impedance for the single copper bar example.

- 1) 3D-PEEC-UNIFORM denotes the full-wave volumetric PEEC solution obtained with a uniform mesh resulting in 1275 nodes and 4680 inductive branches;
- 2) 3D-PEEC-NON-UNIFORM denotes the full-wave volumetric PEEC solution obtained with a nonuniform mesh resulting in 2989 nodes and 14 400 inductive branches in which the smallest element size is 1 μm ;
- 3) 3D-PEEC-NON-UNIFORM-2 denotes the full-wave volumetric PEEC solution obtained with a nonuniform mesh resulting in 7381 nodes and 31 360 inductive branches in which the smallest element size is again 1 μm ;
- 4) S-PEEC denotes the full-wave surface PEEC solution obtained with a uniform mesh resulting in 834 nodes and 2256 surfaces; and
- 5) QS Q3D denotes the quasi-static R-L solution obtained with the commercial software ANSYS Q3D Extractor.

From Fig. 5, it can be seen that the S-PEEC method achieves a high accurate result with a reduced number of unknowns compared to the various volumetric PEEC solvers. However, the S-PEEC requires further investigation: 1) in terms of accuracy at lower frequencies, when the E field and the H field have a divergence-free and a curl-free part that scale differently leading

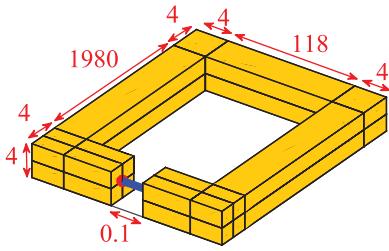


Fig. 6. Test example: Rectangular copper loop (all dimensions are in μm).

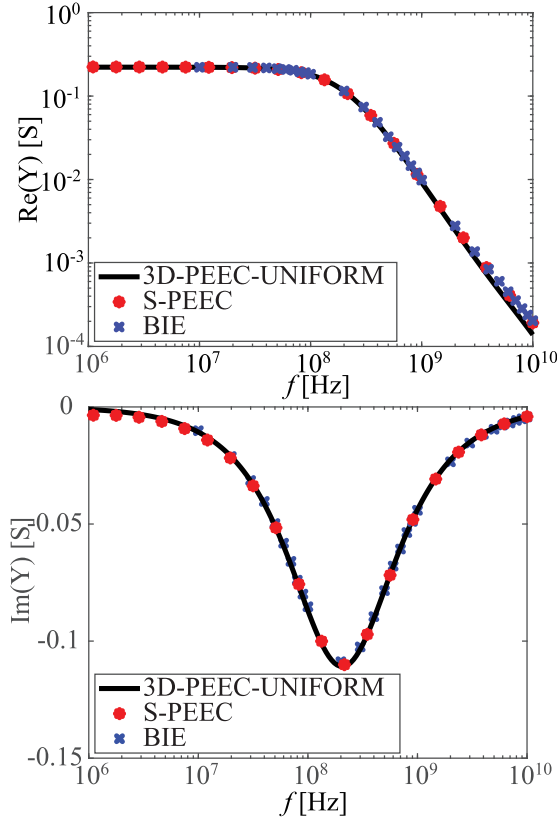


Fig. 7. Port impedance for the rectangular copper loop example comparing the full-wave volumetric PEEC solution, the proposed full-wave surface PEEC solution, and the results obtained with the technique presented in [12].

to large numerical error when one part dominates the other one; 2) the numerical integration, required to fill the coefficients for the internal problem in which the Taylor expansion approach cannot be used as reported in Fig. 3, is extremely slow. Both challenges will be addressed in the future work based on a specialized technique for solving the surface–surface integrals in a faster semi-analytical fashion.

C. Rectangular Loop Example

In this example, a rectangular copper loop is considered in order to compare the accuracy of the developed S-PEEC modeling approach to the boundary integral method presented in [12]. The rectangular copper loop is depicted in Fig. 6, where the blue line represents a lumped current port. The port impedance, evaluated through different methods, is shown in Fig. 7, where

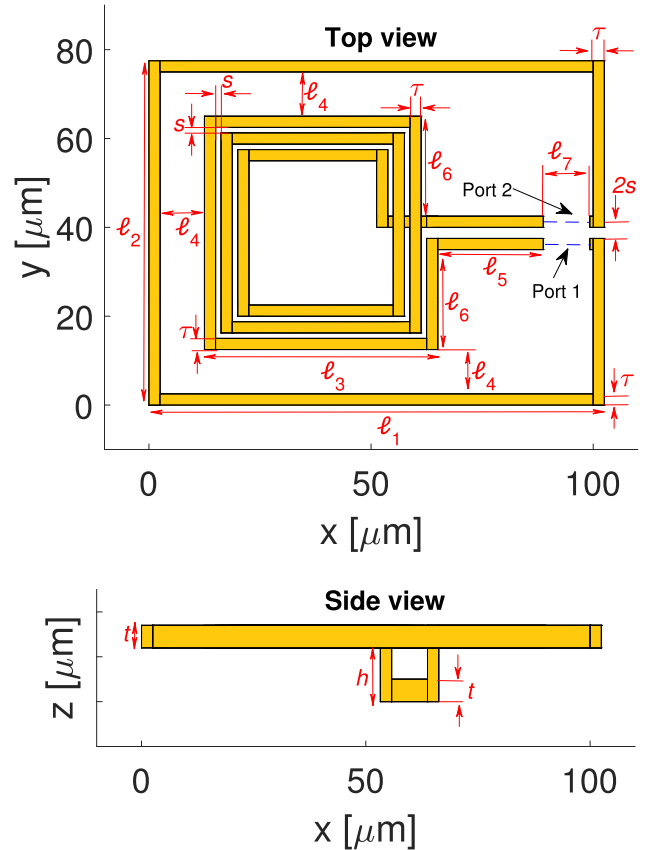


Fig. 8. Test example: Two-port inductor. The dimensions are as follows: $s = 1.25$, $\tau = 2.5$, $t = 1$, $h = 1.75$, $l_1 = 102.5$, $l_2 = 77.5$, $l_3 = 52.5$, $l_4 = 10$, $l_5 = 23.75$, $l_6 = 22.5$, and $l_7 = 10.5$ (all dimensions are in μm).

- 1) 3D-PEEC-UNIFORM denotes the full-wave volumetric PEEC solution obtained with a uniform mesh resulting in 370 nodes and 1144 inductive branches;
- 2) S-PEEC denotes the full-wave surface PEEC solution obtained with a uniform mesh resulting in 364 nodes and 1064 surfaces; and
- 3) BIE (boundary integral equation) denotes the full-wave solution obtained with the technique proposed in [12].

The S-PEEC has a comparable accuracy with respect to the 3D-PEEC-UNIFORM and the BIE, as can be seen in Fig. 7. As the numerical integration used for the internal modeling domain slows down the computational speed as previously mentioned, the PEEC mesh was optimized for the maximum frequency of 10 GHz in order to speed up the calculation.

D. Two-Port Inductor Example

As third example, with the aim to directly compare the accuracy of the developed S-PEEC modeling approach to the surface integral formulation presented in [9], a two-port inductor is investigated. Its geometry is shown in Fig. 8 where the dashed blue lines represent the lumped current ports.

The scattering parameters, with a reference impedance of 50Ω , are evaluated by means of three different methods.

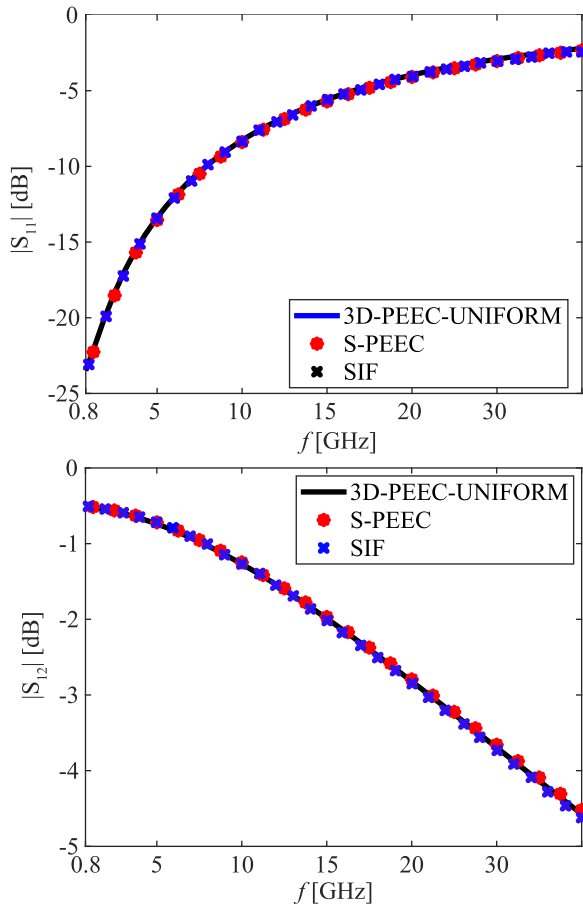


Fig. 9. Port impedance for the rectangular copper loop example comparing the full-wave volumetric PEEC solution, the proposed full-wave surface PEEC solution, and the results obtained with the technique presented in [9].

- 1) 3D-PEEC-UNIFORM denotes the full-wave volumetric PEEC solution obtained with a uniform mesh resulting in 222 nodes and 696 inductive branches.
- 2) S-PEEC denotes the full-wave surface PEEC solution obtained with a uniform mesh resulting in 220 nodes and 728 surfaces.
- 3) SIF (surface integral formulation) denotes the full-wave solution obtained with the technique proposed in [9].

The results are shown in Fig. 9, demonstrating a satisfactory agreement between all the methods.

V. CONCLUSION

In this article, analytical formulas for the computation of the interaction integrals occurring in the S-PEEC formulation have been proposed. Based on the Taylor expansion of the Green's function, analytical formulas are derived for the coefficients of the resulting expansion up to the third order. Their range of applicability to preserve the accuracy is discussed in terms of frequency, size of the mesh, and distances. Impressive speed-ups have been found in the computation of partial elements as a consequence of the analytical forms. Three test cases taken from

the literature have been presented, confirming the accuracy of the proposed approach compared to other methods. The main focus of the present article has been the accuracy and the computational efficiency of the interaction integrals.

REFERENCES

- [1] J. L. Volakis, A. Chatterjee, and L. C. Kempel, *Finite Element Method Electromagnetics: Antennas, Microwave Circuits, and Scattering Applications*, Ser. IEEE Press Series on Electromagnetic Wave Theory, Hoboken, NJ, USA: Wiley, 1998.
- [2] M. Al-Qedra, J. Aronsson, and V. Okhmatovski, "A novel skin-effect based surface impedance formulation for broadband modeling of 3-D interconnects with electric field integral equation," *IEEE Trans. Microw. Theory Techn.*, vol. 58, no. 12, pp. 3872–3881, Dec. 2010.
- [3] S. Omar and D. Jiao, "A new volume integral formulation for broadband 3-D circuit extraction in inhomogeneous materials with and without external electromagnetic fields," *IEEE Trans. Microw. Theory Techn.*, vol. 61, no. 12, pp. 4302–4312, Dec. 2013.
- [4] F. Sheikh Hosseini Lori, A. Menshov, R. Gholami, J. B. Mojolagbe, and V. I. Okhmatovski, "Novel single-source surface integral equation for scattering problems by 3-D dielectric objects," *IEEE Trans. Antennas Propag.*, vol. 66, no. 2, pp. 797–807, Feb. 2018.
- [5] A. E. Ruehli, "Inductance calculations in a complex integrated circuit environment," *IBM J. Res. Dev.*, vol. 16, no. 5, pp. 470–481, Sep. 1972.
- [6] A. E. Ruehli and P. A. Brennan, "Efficient capacitance calculations for three-dimensional multiconductor systems," *IEEE Trans. Microw. Theory Techn.*, vol. 21, no. 2, pp. 76–82, Feb. 1973.
- [7] A. E. Ruehli, "Equivalent circuit models for three dimensional multiconductor systems," *IEEE Trans. Microw. Theory Techn.*, vol. MTT-22, no. 3, pp. 216–221, Mar. 1974.
- [8] A. E. Ruehli, G. Antonini, and L. Jiang, *Circuit Oriented Electromagnetic Modeling Using the PEEC Techniques*. Hoboken, New Jersey: Wiley-IEEE Press, 2017.
- [9] U. R. Patel, S. Sharma, S. Yang, S. V. Hum, and P. Triverio, "Full-wave electromagnetic characterization of 3-D interconnects using a surface integral formulation," in *Proc. IEEE 26th Conf. Elect. Perform. Electron. Packag. Syst.*, Oct. 2017, pp. 1–3.
- [10] X. Sun, T. Huang, L. Ye, Y. Sun, S. Jin, and J. Fan, "Analyzing multiple vias in a parallel-plate pair based on a nonorthogonal PEEC method," *IEEE Trans. Electromagn. Compat.*, vol. 61, no. 5, pp. 1602–1611, Oct. 2019.
- [11] L. Ye *et al.*, "Modeling stripline with slotted ground plane in multilayered circuit board using PEEC formulation," *IEEE Trans. Electromagn. Compat.*, vol. 62, no. 1, pp. 280–284, Feb. 2020.
- [12] M. Huynen *et al.*, "Entire domain basis function expansion of the differential surface admittance for efficient broadband characterization of lossy interconnects," *IEEE Trans. Microw. Theory Techn.*, vol. 68, no. 4, pp. 1217–1233, Apr. 2020.
- [13] J. Peeters, I. Bogaert, and D. De Zutter, "Calculation of MoM interaction integrals in highly conductive media," *IEEE Trans. Antennas Propag.*, vol. 60, no. 2, pp. 930–940, Feb. 2012.
- [14] A. Rong, A. C. Cangellaris, and L. Dong, "Comprehensive broadband electromagnetic modeling of on-chip interconnects with a surface discretization-based generalized PEEC model," in *Proc. Elect. Perform. Electron. Packag.*, Oct. 2003, pp. 367–370.
- [15] Y. Wang, V. Jandhyala, and C. J. R. Shi, "Coupled electromagnetic-circuit simulation of arbitrarily-shaped conducting structures," in *IEEE 10th Topical Meeting Elect. Perform. Electron. Packag.*, Oct. 2001, pp. 233–236.
- [16] D. Gope, A. E. Ruehli, C. Yang, and V. Jandhyala, "(s)PEEC: Time- and frequency-domain surface formulation for modeling conductors and dielectrics in combined circuit electromagnetic simulations," *IEEE Trans. Microw. Theory Techn.*, vol. 54, no. 6, pp. 2453–2464, Jun. 2006.
- [17] C. A. Balanis, *Advanced Engineering Electromagnetics*. New York, USA: John Wiley and Sons, 1989.
- [18] A. Poggio and E. Miller, "Computer Techniques for Electromagnetics," in *Integral Equation Solutions for Three Dimensional Scattering Problems*. New York, NY, USA: Pergamon, 1973.
- [19] S. Seppo Järvenpää, M. Taskinen, and P. Ylä-Oijala, "Singularity extraction technique for integral equation methods with higher order basis functions on plane triangles and tetrahedra," *Int. J. Numer. Methods Eng.*, vol. 58, no. 8, pp. 1149–1165, Oct. 2003.

- [20] S. Chakraborty and V. Jandhyala, "Evaluation of Green's function integrals in conducting media," *IEEE Trans. Antennas Propag.*, vol. 52, no. 12, pp. 3357–3363, Dec. 2004.
- [21] S. Chakraborty and V. Jandhyala, "Surface-based broadband electromagnetic-circuit simulation of lossy conductors," *IEE Proc. Microw. Antennas Propag.*, vol. 153, no. 2, pp. 191–198, Apr. 2006.
- [22] M. Taskinen, "On the fully analytical integration of singular double integrals arising from the integral equation methods," in *CEM'11 Comput. Electromagn. Int. Workshop*, Aug. 2011, pp. 13–18.
- [23] Y. Jiang and K. Wu, "Quasi-static surface-PEEC modeling of electromagnetic problem with finite dielectrics," *IEEE Trans. Microw. Theory Techn.*, vol. 67, no. 2, pp. 565–576, Feb. 2019.
- [24] H. Wang and J. Fan, "Modeling local via structures using innovative PEEC formulation based on cavity Green's functions with wave port excitation," *IEEE Trans. Microw. Theory Techn.*, vol. 61, no. 5, pp. 1748–1757, May 2013.
- [25] L. Lombardi, G. Antonini, and A. E. Ruehli, "Analytical evaluation of partial elements using a retarded Taylor series expansion of the Green's function," *IEEE Trans. Microw. Theory Techn.*, vol. 66, no. 5, pp. 2116–2127, May 2018.
- [26] C. Wollenberg and A. Gurisch, "Analysis of 3-d interconnect structures with PEEC using SPICE," *IEEE Trans. Electromagn. Compat.*, vol. 41, no. 4, pp. 412–417, Nov. 1999.
- [27] P. J. Restle, A. E. Ruehli, S. G. Walker, and G. Papadopoulos, "Full-wave PEEC time-domain method for the modeling of on-chip interconnects," *IEEE Trans. Comput.-Aided Design Integr. Circuits Syst.*, vol. 20, no. 7, pp. 877–886, Jul. 2001.
- [28] L. Lombardi, D. Romano, and G. Antonini, "Partial element equivalent circuit method modeling of silicon interconnects," *IEEE Trans. Microw. Theory Techn.*, vol. 65, no. 12, pp. 4794–4801, Dec. 2017.
- [29] K. M. Chen, "A mathematical formulation of the equivalence principle," *IEEE Trans. Microw. Theory Techn.*, vol. 37, no. 10, pp. 1576–1581, Oct. 1989.
- [30] L. Lombardi, D. Romano, and G. Antonini, "Analytical formula for the magnetic-to-electric field coupling of magnetization in the partial element equivalent circuit method," *IEEE Trans. Magn.*, vol. 54, no. 10, pp. 1–12, Oct. 2018.
- [31] A. W. Glisson, "Electromagnetic scattering by arbitrarily shaped surfaces with impedance boundary conditions," *Radio Sci.*, vol. 27, no. 11, pp. 935–943, 1992.
- [32] B. Gustavsen and A. Semlyen, "Rational approximation of frequency domain responses by vector fitting," *IEEE Trans. Power Appl. Syst.*, vol. 14, no. 3, pp. 1052–1061, Jul. 1999.
- [33] I. Kovacevic-Badstuebner, D. Romano, L. Lombardi, U. Grossner, J. Ekman, and G. Antonini, "Accurate calculation of partial inductances for the orthogonal PEEC formulation," *IEEE Trans. Electromagn. Compat.*, early access, May 11, 2020, doi: [10.1109/TEMC.2020.2986933](https://doi.org/10.1109/TEMC.2020.2986933).
- [34] M. Lucido, M. D. Migliore, and D. Pinchera, "A new analytically regularizing method for the analysis of the scattering by a hollow finite-length PEC circular cylinder," *Prog. Electromagn. Res. B*, vol. 70, no. 7, pp. 55–71, 2016.
- [35] MATLAB version 9.8.0.1417392 (R2020a). Natick, MA, USA: The Mathworks, Inc., 2020.



Francesca Di Murro received the Laurea degree in telecommunications engineering, and the Ph.D. degree in electrical engineering and information from the University of Cassino and Southern Lazio, in 2010 and 2016, respectively, where she has studied the applications of semi-analytical methods for the analysis of electromagnetic scattering. In 2019, she was a Research Fellow with the University of Luleå, and in 2020 at the University of L'Aquila. Her current research interests include the field of scattering and integral equations.



Daniele Romano was born in Campobasso, Italy, in 1984. He received the Laurea degree in computer science and automation engineering in 2012, and the Ph.D. degree in industrial engineering, computer science, and economics in 2018, both from the University of L'Aquila, Italy.

Since 2012, he has been with the UAq EMC Laboratory, University of L'Aquila, focusing on EMC modeling and analysis, algorithm engineering, and speed-up techniques applied to EMC problems.



Maria De Lauretis (Senior Member, IEEE) received the M.E. degree in computer science and automation engineering from the University of L'Aquila, L'Aquila, Italy, in 2012, and the Ph.D. degree in industrial electronics from the Luleå University of Technology, Luleå, Sweden, in 2018.

She is currently a Postdoctoral Fellow with the Computer Science, Electrical and Space Department, Luleå University of Technology. Her research interests include multiconductor transmission lines, electromagnetic structure modeling, and power converters.



Ivana Kovacevic-Badstuebner (Member, IEEE) received the Ph.D. degree in electrical engineering from ETH Zurich, Switzerland, in 2012.

From 2008 to 2015, she was with the Power Electronics Systems (PES) Laboratory, ETH Zurich. In March 2016, she joined the Advanced Power Semiconductor (APS) Laboratory at ETH Zurich. Her research interests include novel packaging technologies for SiC power devices, the optimization of power module layout with respect to electromagnetic interference, and multidomain modeling of power semiconductor devices and their modules.



Luigi Lombardi received the Laurea degree (M.D.) in electronic engineering and the Ph.D. in industrial engineering, computer science, and economics, both cum laude, from the University of L'Aquila, L'Aquila, Italy, in 2015 and 2019, respectively.

In early 2018, he was a Visiting Researcher with the Department of Electronics, Carleton University, Ottawa, ON, Canada. Since November 2018, he has been working as a Design Engineer with the Non Volatile Memory Design Team, Micron Semiconductor, Avezzano, Italy.



Ulrike Grossner received the Dipl.-Phys. and the Dr. rer. nat. degree from the Friedrich-Schiller University, Jena, Germany, in 1997 and 2000, respectively.

In 2014, she was a Full Professor with ETH Zurich, Switzerland, where she established the Advanced Power Semiconductor Laboratory (APS), working on devices and packaging for advanced power semiconductors.



Jonas Ekman (Member, IEEE) was born in Boden, Sweden, in 1972. He received the Ph.D. degree in electrical engineering from the Luleå University of Technology, Sweden, in 2003.

From 2003 to 2007, he was a Researcher with the Luleå University of Technology. During 2005 and 2006, he did his postdoctoral research in full-wave, time domain, and PEEC modeling at the EMC Laboratory, University of L'Aquila, Italy. In 2014, he was appointed Professor with the Luleå University of Technology. His research interests include compu-

tational electromagnetics, in particular, the use of the PEEC method for realistic electromagnetic modeling.



Giulio Antonini (Senior Member, IEEE) received the laurea degree (*cum laude*) from the University of L'Aquila, L'Aquila, Italy, in 1994 and the Ph.D. degree from the University of Rome "La Sapienza," in 1998, both in electrical engineering.

Since 1998, he has been with the UAq EMC Laboratory, University of L'Aquila, where he is currently a Professor. He has coauthored the book *Circuit Oriented Electromagnetic Modeling Using the PEEC Techniques* (Wiley-IEEE Press, 2017). His research interests include the field of computational electromagnetics.



Fabrizio Frezza (Senior Member, IEEE) received the Laurea degree (*cum laude*) in electronic engineering, and the doctorate degree in applied electromagnetics and electrophysical sciences from "La Sapienza" University of Rome, Italy, in 1985 and 1991, respectively.

In 1986, he joined the Department of Electronics of the same University, where he was Researcher from 1990 to 1998, temporary Professor of Electromagnetic Fields from 1994 to 1998, Associate Professor from 1998 to 2004, and he has been a Full Professor of

Electromagnetic Fields since 2005. His research activity has concerned guiding structures, antennas, and resonators for microwaves and millimeter waves, numerical methods, scattering, optical propagation, plasma heating, anisotropic media, artificial materials and metamaterials, and cultural-heritage applications.

Prof. Frezza is a Member of Sigma Xi and Senior Member OSA.